INSTITUTE OF PHYSICS PUBLISHING JOURNAL OF MICROMECHANICS AND MICROENGINEERING

J. Micromech. Microeng. **15** (2005) 20–28 PII: S0960-1317(05)78812-4

Milling yield estimation in focused ion beam milling of two-layer substrates

Ampere A Tseng[1], **Ivan A Insua**[1], **Jong-Seung Park**[1] **and Chii D Chen**[2]

[1] Department of Mechanical and Aerospace Engineering, Center for Solid State Electronics Research, Arizona State University, Box 876106, Tempe, AZ 85287-6106, USA
[2] Institute of Physics, Academia Sinica, Taipei 11529, Taiwan, Republic of China

E-mail: ampere.tseng@asu.edu

Received 5 April 2004, in final form 25 August 2004
Published 1 October 2004
Online at stacks.iop.org/JMM/15/20
doi:10.1088/0960-1317/15/1/004

Abstract

The material removal rate or milling yield of using the focused ion beam (FIB) for milling two-layer substrates is studied. The preparation of the two-layer substrate is first presented and is followed by the procedure on conducting the milling experiment. The effects of the dwell time on the milling rate and the final profiles of the milled structures are investigated. The atomic force microscope (AFM) is applied for measuring the profiles of the milled channels. Based on the AFM measurements, a relatively simple formula is developed to estimate the milling yield, which is normally dictated by both the characteristics of sputtering and redeposition for channel milling. The estimated milling rates are then compared with the corresponding sputtering yields predicted using a different numerical scheme. The milling rates obtained presently are discovered to be roughly equal to the predicted normal-incidence sputtering yields for both layers involved. Consistency is found as the present findings are compared with other milling studies on single-layer substrates. Finally, concluding remarks that summarize the present work and suggest future work on FIB milling are included.

(Some figures in this article are in colour only in the electronic version)

1. Introduction

In the semiconductor industry, the focused ion beam (FIB) has been a valuable tool for photomask repairing, metallic line mending of integrated circuits, semiconductor doping, surface probing of substrate materials and lithography (Reyntjens and Puers 2001, Tseng 2004). Because of the very short wavelength and very large energy density, the focused ion beam has the ability for direct fabrication of structures that have feature sizes at or below 1 μm; as a result, the FIB has recently become a popular candidate in making high quality microdevices or high precision microstructures, including microgears (Fu *et al* 2000), micromolds (Vasile *et al* 1997), microprobes (Hopkins *et al* 1995), microtools (Picard *et al* 2003) and optical elements (Chyr *et al* 1999, Stanishevsky 1999).

In this paper, the capability of using the FIB for milling a two-layer substrate, which consists of a gold layer coated on top of a silicon layer, is presented. The gold-coated Si substrate has been of considerable interest for micro- and nano-device fabrication. Not only does the gold layer provide excellent electrical connection among circuit elements, it can also be an integral part of the devices, such as in Schottky diodes and devices for interconnections, without suffering from electromigration effects (Ghandhi 1994). Moreover, gold-coated silicon substrates become especially useful in fabrication of nanoscale structures. Self-assembled monolayers can be formed on a gold film coated on a Si substrate using a photopatterning process (Creager *et al* 1992, Huang *et al* 1994). Whitesides and Love (2001) have developed a soft lithography technique to print a patterned organic molecule layer onto a gold-coated Si substrate to form

a self-assembled monolayer as a building block for three-dimensional nanostructures. The self-assembled monolayer pattern can be as thin as 50 nm.

Recently, the Si substrate with an Au layer has become extremely popular in wafer-level packaging, because of the excellent bonding capability of gold with Si using the eutectic bonding technique (Dragoi *et al* 2003, Hsu and Clatterbaugh 2004). Also, since gold and other face-centered cubic metals, including Al, Cu and Ge, have high diffusion coefficients at relatively low temperatures, reliable Au/Al, Au/Cu and Au/Ge wafer-level bonds can be created at temperatures below 450 °C (Takano *et al* 1997, Iida *et al* 1997, Budraa *et al* 1999, Dragoi *et al* 2003). In many applications, since only non-brittle mixtures can be formed by the diffusion in the interface, a diffusion bond is preferable over other bonds, including intermetallic and eutectic, in which undesirable brittle intermetallic or eutectic alloys are normally formed in the interface. Gold can also form good eutectic bonds with Si and Sn. Moreover, by taking the advantages of both the transparency of silicon and gold's good absorbing ability at infrared and x-ray wavelengths, the gold-coated Si substrate has been used for infrared-laser and x-ray masks for micro- and nano-lithography (Dauksher *et al* 1994). Consequently, the ability for patterning gold-coated Si substrates is important for further advances in the fabrication of both micro- and nano-devices.

Furthermore, two-layer milling is critical to mask making, because masks are typical two-layer structures; while the top layer serves as an absorber or a blocker, the bottom layer can serve as a transparent holder. The feature size of the mask is largely dictated by the milling dimensions at the interface. As a result, one of the purposes of the present study is to find the correlation between the channel mouth width and the interface width as well as the relationship between this correlation and the major operating parameters of FIB milling.

In the present research, the FIB milling experiments will be conducted by changing the dwell time to obtain different submicron channel structures on gold-coated Si substrates. The preparation of the gold-coated Si substrates will be described first while the impact of the coating process on surface quality will also be evaluated. Submicron channels will then be milled by a 90 keV As^{2+} FIB and the resulting profiles will be measured using the atomic force microscope (AFM). Based on these AFM measurement data, the milling yields for making these channels will be estimated and compared with the numerically predicted sputtering yield using a different scheme. This comparison provides the benchmark value for further discussion and explanation of the experimental results. Comparison of the present findings with other nano- and micro-channel milling studies will also be included and used to assess the effectiveness of the process used for milling sub-microstructures.

2. Milling experiments

The FIB machine adopted is Model 150, manufactured by Nanofab of Columbia, MD. The machine is equipped with a source-auto-align controller to compensate the source spatial drift and with a closed-loop servo to stabilize the long-term drift current to within 1% (or 1 pA). The ion column and the work chamber are differentially cryopumped and vibration isolated. The machine has three selectable apertures, and computer-controlled electrostatic lenses and hardware to control the beam size. The beam is close to a Gaussian profile. The beam profile and size can be calibrated or fine tuned by using a Faraday cup detector or by measuring the current density profile in milling a spot on a pre-calibrated flat sample. In fact, the roundness of the beam can be directly determined by examining the roundness of the milled shape. The machine had been calibrated before conducting the present experiment.

The PdAsB alloy is used as the source to provide the arsenic 2+ ion beam for milling various submicron channels. The micro- and nano-channel structures have been widely used for many micro- and nano-electromechanical systems (M/NEMS), including micro heat pipes, biosensors and detectors, thermal microreactors, microfluidic devices, optical waveguides and molecular electronics (Tseng *et al* 2000, Madou 2002). The channel structures are fundamental building blocks for these micro-components or devices and are analogous to wires or thin film electrical interconnects in conventional integrated circuits. These devices and components have broad applications in the aerospace, automotive, medical, pharmaceutical, instrument, electronic and many other industries.

2.1. Substrate preparation

The target material for the present study is a two-layer substrate consisting of a gold layer of 60 nm thick on a single-crystal silicon wafer. The gold layer is coated by a high vacuum evaporation system with an ion-pumped glass belljar capable of $\sim 6 \times 10^{-7}$ Torr. While the equilibrium melting temperature of gold is 1063 °C, the gold was melted at 1132 °C to attain a vapor pressure of 10^{-4} Torr, which is suitable for deposition. System pressures were monitored by ion and thermal conductivity gauges while the film thickness was measured by a quartz-crystal thickness monitor. The substrate stage is either water/liquid nitrogen cooled or resistance-heated. A thermocouple in the stage indicates the substrate temperature.

Recently, the vacuum evaporation technique for coating gold on Si substrate has been studied by many investigators, including Golan *et al* (1992), Hammiche *et al* (1994), Levlin *et al* (1997) and Semaltianos and Wilson (2000). They have indicated that the quality of the coated layer is mainly dependent on the target temperature and evaporation rate. For instance, at room temperature, evaporated gold layers may present a rolling-hill morphology while a higher temperature may affect its surface roughness, with a rough hill-like surface but a more homogeneous grain-size distribution (Golan *et al* 1992, Semaltianos and Wilson 2000). In fact, the surface roughness and grain-size homogeneity can greatly affect the potential applications of the gold-coated Si substrates. For example, the surface roughness has a strong impact on the quality of diffusion and eutectic bonding (Dragoi *et al* 2003) and on the monolayers created by molecular self-assembly (Creager *et al* 1992). Also, the surface roughness is essential in the evaluation of the milling effectiveness. Consequently, the effect of the target temperature and the evaporation rate on the surface roughness will be evaluated.

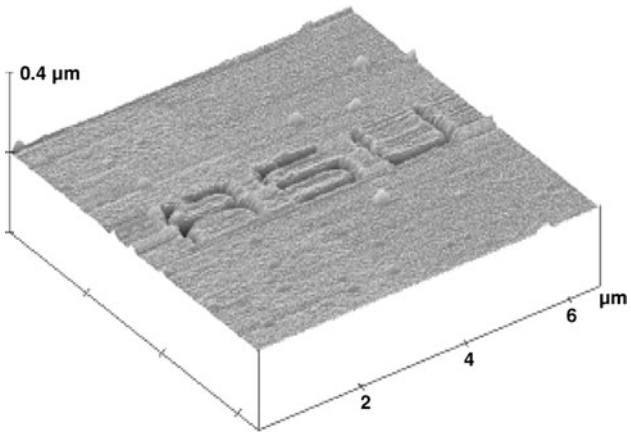

Figure 1. AFM image of gold layer coated at 25 °C having typical surface roughness (R_q) of 1.8 nm and 'ASU' pattern milled with 50 ms dwell time.

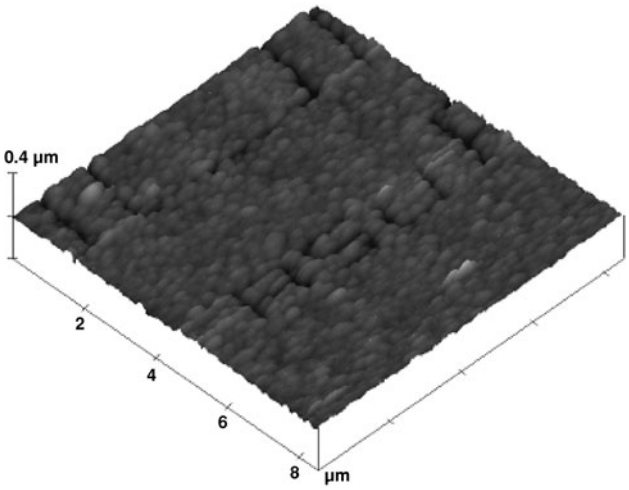

Figure 2. AFM image of gold layer coated at 360 °C having typical surface roughness (R_q) of 11.3 nm and 'ASU' pattern milled with 50 ms dwell time.

In the present study, two substrate temperatures, 25 and 360 °C, at two evaporation rates, 0.02 and 0.06 nm s^{-1}, are considered for depositing the gold layers. After evaporation, the surface roughness of the gold layers is measured by the AFM to quantify the surface quality. At the substrate temperature of 25 °C, the typical root-mean-square surface roughness (R_q) is 1.8 nm and showed no significant change for the deposition speed increasing from 0.02 to 0.06 nm s^{-1}. This roughness value is also consistent with that of the silicon substrate, on the order of 1 nm. However, for the substrate temperature elevating from 25 °C to 360 °C, the roughness increases more than sixfold to R_q = 11.3 nm with an evaporation rate of 0.02 nm s^{-1}. The present results indicate that the surface roughness of the evaporated gold layer increases with the substrate temperature, which is consistent with those reported by Golan *et al* (1992) and Semaltianos and Wilson (2000). The AFM surface images for the samples at 25 °C and 360 °C are shown in figures 1 and 2, respectively. Although the images shown in both figures were taken after the sample was milled, the surface appearance can clearly be observed from those outside the milled regions. It can be observed from figure 2 that the milled pattern 'ASU' is barely noticeable and the channel is rough and resembles more of a ditch. Obviously, this level of roughness would cause inconsistent measurements in quantifying the dimensions of milled channels because the roughness is on the same order of magnitude as the feature sizes of the milled channels. Consequently, only the results based on the gold layer evaporated at 25 °C are reported.

2.2. Sputtering yield prediction

Because the arsenic ion source is not often used for milling, reliable experimental data on its milling yield on gold targets are still not available. To provide guidance for the milling experiment and a basis for examining the experimental results, a numerical prediction of the effects of the incident angle on the sputtering yield is conducted. The software package, TRansport of Ions in Matter (TRIM), is used. TRIM is a comprehensive program that uses a Monte Carlo treatment of ion–atom collisions and the surface binding energies are

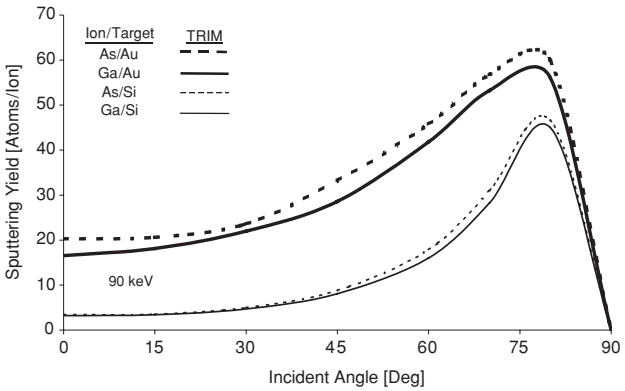

Figure 3. Angular dependence of sputtering yields of 90 keV As and Ga ions on Au and Si targets.

used for the simulation of the sputter yield of Au and Si (Biersack and Haggmark 1980, Ward 1985). Since TRIM is based on the Monte Carlo method, the number of ions used in the simulation can have an effect on the results. Normally, the TRIM predictions become converged when the ion number surpasses 500. To be conservative, 1000 ions are used for all of the TRIM simulations presented here.

Figure 3 shows the results of the TRIM simulations of the dependence of the sputtering yield on the incident angle at an ion energy of 90 keV for Au and Si substrates. For the sake of comparison, in addition to the As ion, the Ga ion is also included in the simulation since the Ga ion is the most popular ion species selected for FIB milling and its data will be used in result discussion. For all cases considered, the increase in incidence angle raises the sputtering yield until it reaches its maximum near 80°; then it decreases very rapidly to zero as the incident angle approaches 90°. As shown in figure 3, at the normal incidence, the sputtering yield of the Au substrate is more than six times higher than that of the Si substrate; however, the sputtering yield of the Si substrate increases about 10 times from the normal incidence to the angle at its peak while the corresponding sputtering yield for the Au substrate increases less than 2.5 times. The behavior of

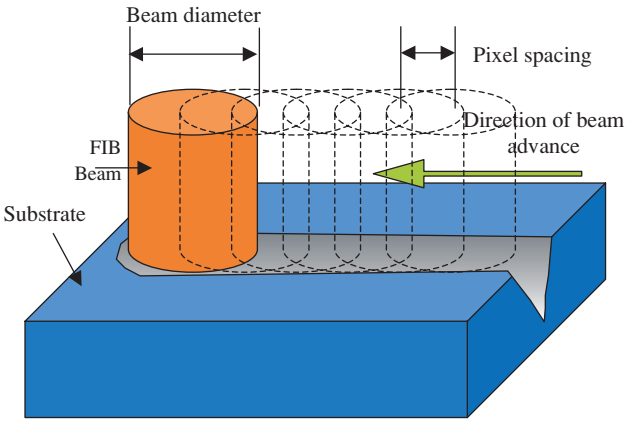

Figure 4. The schematic of FIB milling.

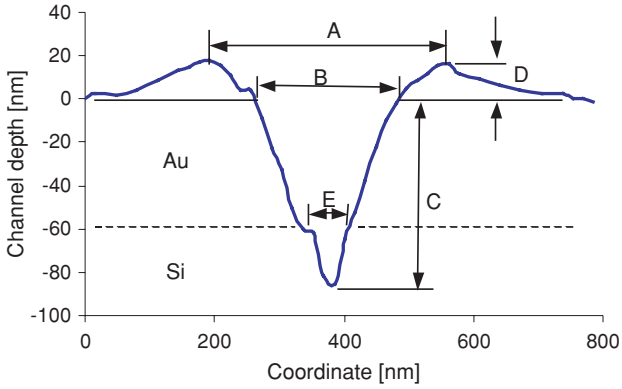

Figure 5. Channel feature definition and AFM measurement of typical channel profile milled with 40 ms dwell time.

the angular dependence of sputtering yields has been observed by many researchers, including Santamore *et al* (1997) and Frey *et al* (2003).

Also, since the atomic weight of an $^{74.92}$As ion is slightly heavier than that of a $^{69.72}$Ga ion, the sputtering yield of As is slightly higher than that of Ga. In general, heavier ions can produce higher sputtering yields. Although the data are not shown, in most the cases, the sputtering yield either levels off or decreases sometimes for ion energies higher than 100 keV because implantation becomes the dominating factor in the interaction between the ions and the target at higher energies (Ghandhi 1994, Tseng 2004).

2.3. Milling operation

A 90 keV As^{2+} FIB with a beam current of 5 pA is selected in the present study. The pixel spacing (p_s) is set at 14.5 nm and the beam's full width at half maximum (FWHM) diameter (d_f) is set at 50 nm. As mentioned earlier, the FIB machine had just been calibrated before conducting the present experiment; the setting of the operation conditions should be reliable. Using raster scanning, the milling is performed by a precise pixel-by-pixel movement and is schematically shown in figure 4. To mill smooth channel structures, the ion intensity rate or ion flux with respect to the scanning direction has to be uniform or unwavering. To achieve this, the pixel spacing must be small enough to allow a proper overlap between adjacent pixels so that a smooth uniform profile can be milled. In the present milling condition, the corresponding ratio of the pixel spacing to the beam diameter (p_s/d_f) is 0.29, which is smaller than the threshold value, i.e., 0.637 (Tseng *et al* 2004), which means the scanning ion intensity or flux should be steady and uniform in the milling direction.

In milling, each channel pattern is milled by a single scan (pass) and the dwell time is varied from 5 to 50 ms. Each pattern consists of three sets of 'ASU' with different character sizes. The largest character is 5 μm $\times$ 5 μm while the smallest character is 1 μm $\times$ 1 μm. The AFM image of an 'ASU' pattern milled with a 50 ms dwell time has been shown in figure 1, where the channel mouth is about 300 nm wide. A typical cross-sectional profile milled with a 40 ms dwell time is shown in figure 5. It possesses a V-shaped cross-section with a maximum depth of 86 nm at the center and

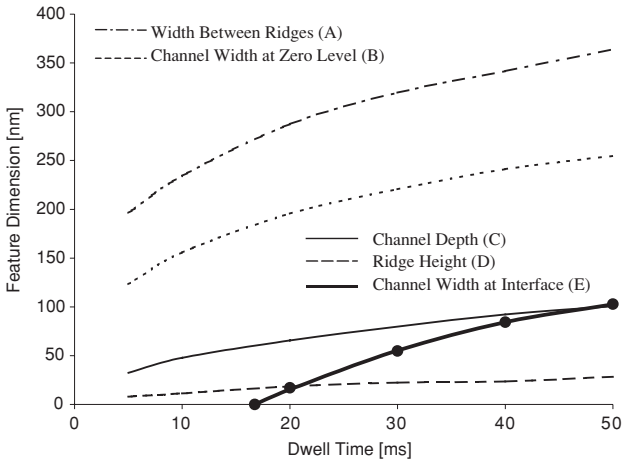

Figure 6. Channel feature measurements with correlation of channel width at interface.

maximum width at the mouth. Since the gold layer is 60 nm thick, the channel penetrates through the gold layer into the silicon layer. Occasionally, also shown in figure 5, the cross-sectional profile has a 'stair-step' change near the interface, which may reflect the discontinuity of the material properties across the interface. It is believed that this change may be caused by the fact that silicon is much more difficult than gold to be sputtered, as shown in figure 3, or the fact that a weak interface bonding occurs in the measured region. Sometimes, the interface bonding is not as strong as the bonded materials.

Figure 5 also illustrates the definition of the five features that are used to characterize the profile of the V-shaped channel: A is the ridge width which is the distance between the ridge peaks, B is the mouth width which is the channel width with respect to the original surface, C is the depth from the original surface, D is the ridge height and E is the channel width at the interface between two layers. Ridges that are formed along the channel banks are mainly created by redeposition.

2.4. Profile measurements

Figure 6 shows the measurement results of the five profile features of the milled channel versus the dwell time (the amount of ion dose). The features of A, B, C and D are plotted

in continuous curves using curve fitting techniques, while the data for feature E are depicted directly as solid dots, since the interface width data (E) are needed for further milling yield estimation. The data for each dwell time shown in the figure are the mean of more than 100 AFM measurements. The corresponding standard deviations are approximately 10% of their mean and the milled trench can indeed be considered to be uniform along the milling direction. It is believed that the main reasons for causing the 10% standard deviations are due to the random nature of the redeposition in milling and the instability and the drift of the beam current.

Furthermore, to have consistent results in measurement, each datum is taken on a location (randomly selected) at least 300 nm away from any turning corners of the patterns to minimize the turning effects. Also, to establish the reliability of the measurements, the profiles of the milled trenches are examined by two types of scanning resolutions (E and J Scanners) and two types of tips (17° and 35° half-cone angles) when using the AFM. Since the effect of using these two different tips with two different scanning resolutions on the measurement are insignificant, the data presented in figure 6 should be considered reliable and consistent. The main reason for this insignificant effect on the measurement may be due to the fact that the aspect ratio of the milled trenches considered is not extremely large and both tips can deliver consistent results. A more detailed discussion on the reliability of the AFM measurement may also be found in Tseng *et al* (2004).

As shown in figure 6, although all of the features increase with the dwell time, the increase rates are gradually reduced as the dwell time increases. This may indicate that the influence of the silicon layer grows with the dwell time since the sputtering yield of Si is much smaller than that of Au. As the milling continues or as the dwell time is increased, more Si is sputtered out, and the effect of the lower sputtering yield of the Si layer on the channel feature sizes is larger. As a result, the growing rate of the feature dimensions shown in figure 6 is decreased as the dwell time increases. Also, the measurements indicate that the mouth width (B in figure 6) is about 2–5 times larger than the FWHM beam diameter ($d_f = 50$ nm). This may suggest that at a higher dwell time, the ion intensity outside the FWHM core region has sufficiently high dose to produce sizable sputtering, and this finding is also consistent with those based on one-layer milling (Tseng *et al* 2004).

Both Frey *et al* (2003) and Li *et al* (2003) have recently used a 30 keV Ga^+ FIB to mill nanoscale channels with a single pass on Si substrates. They used different beam diameters at different beam currents and all learned that the channel profiles milled with a single pass are similar to that shown in figure 5, in a 'V' shape. One of the channel profiles milled at 1 pA shown by Li *et al* (2003) is 10 nm deep while its mouth width is around 65 nm. Their results further confirm the present finding that the V-shaped channel profile is the inherent shape obtained by single-scan FIB milling.

3. Milling yield estimation

To quantify the effectiveness of the milling process to the two-layer substrate, the milling yield for each layer is evaluated in this section.

3.1. Material removal

As indicated in figure 5, the channel cross-section is V-shaped. The material removal rate (M) within a specific dwell time (t_d) and pixel spacing (p_s) can be approximated by a wedge shape volume:

$$M = BCp_s/(2t_d) \tag{1}$$

where the cross-section of the channel is approximately $BC/2$ and the values of B and C are shown in figure 6.

Since both materials, Au and Si, can be involved in milling, the material removal rate (M) can be specifically divided into the material removal rate for Si (M_s) and for Au (M_a). If the channel depth in the bottom (Si) layer can be approximated by $C(E/B)$ as indicated in figure 5, the material removal rate of M_s and M_a can be found by following the similar procedure in developing equation (1). One has

$$M_s = CE^2p_s/(2Bt_d) \qquad \text{for} \quad E > 0 \tag{2a}$$

and

$$M_a = M - M_s = C(B^2 - E^2)p_s/(2Bt_d) \qquad \text{for} \quad E \geqslant 0 \tag{2b}$$

where the values of E and C can be found from figure 6. If $E = 0$, it becomes single-layer milling and equation (2b) can be reduced to equation (1). Since Au has a face-centered cubic crystalline structure having four atoms in its unit cell while Si unit cell is a diamond-cubic crystalline structure containing eight atoms, the volume occupied by one atom can be found to be $b_a^3/4$ for Au and $b_s^3/8$ for Si, where b_a and b_s are the lattice parameters of Au and Si, respectively. Thus, based on equation (2), the number of atoms removed from Si and Au substrates, N_s and N_a, can be, respectively, found as

$$N_s = 4CE^2p_s/\left(Bb_s^3\right) \qquad \text{for} \quad E > 0 \tag{3a}$$

and

$$N_a = 2C(B^2 - E^2)p_s/\left(Bb_a^3\right) \qquad \text{for} \quad E \geqslant 0. \tag{3b}$$

It is to be noted that the shape of the milled structures is influenced by the angle dependence of the sputter yield and by the redeposition of sputtered material as mentioned by Tseng (2004). Due to the different angles of incidence and the unequal width of the channel at the surface and at the interface, the dependence of E and B on the dwell time may not be the same. The influence of redeposition on the channel interface width E may be more pronounced than that of the mouth width B. Because of this effect, the values of the depth in the bottom layer could be underestimated. Consequently, the present assumption of the channel depth in the bottom (Si) layer equal to $C(E/B)$ in equation (2a) should be considered as a first-order approximation. More studies on this aspect are needed to provide better approximations, which may depend on both the angles of incidence and the channel shapes at the surface and at the interface. Also, the swelling effects or the density changes due to amorphization in FIB milling are not included in the present formulation. Based on a recent review by Tseng (2004), the effects of amorphization or the amount of swelling should be neglected since the ion dose levels in the present study are too high to produce any noticeable effects.

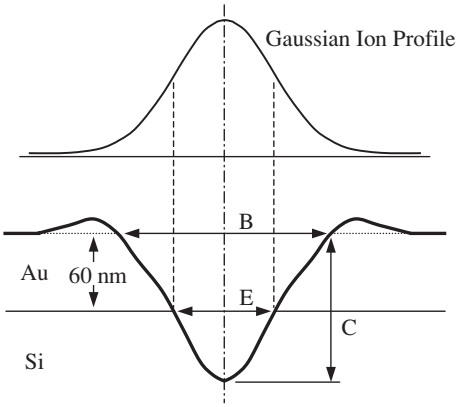

Figure 7. Ion beam profile and its density allocation to Au and Si substrates.

3.2. Ions allocation

To determine the milling yield, the number of ions bombarded on Au and Si should also be obtained. As suggested by most FIB studies, a Gaussian profile is used to represent the ion beam density distribution (D). Mathematically, one can have (Weisstein 1999, Tseng *et al* 2003)

$$D(r,\sigma) = \frac{D_0}{\sigma\sqrt{2\pi}} \exp\left(-\left(\frac{r}{\sigma\sqrt{2}}\right)^2\right) \tag{4}$$

where D_0 is the density constant, r is the radial coordinate and the beam center is located at $r = 0$, and σ is the standard deviation of the Gaussian distribution, in which the beam FWHM diameter (d_f) is equal to 2.35σ. The constant D_0 can be obtained by satisfying the condition in which the total input dose equals the total ions to the target within one dwell time, i.e., $\iint D(r,\sigma) r \, dr \, d\theta = I_p t_d / e$. Thus, one can have (Tseng *et al* 2003)

$$D_0 = (I_p t_d)/[(2\pi)^{1/2} e\sigma] = 0.94[I_p t_d / e d_f] \tag{5}$$

where I_p is the beam current and e is the electric charge equal to 1.60×10^{-19} C for a single-charged ion and 3.20×10^{-19} C for a double-charged ion, such as As^{2+}.

As illustrated in figure 7, it is assumed that the Gaussian distributed ions are impinging on the target normally and the numbers of ions to Au and Si are determined by considering the projection area related to the specific target material. Thus, the total ions impinging on the Si layer (D_s) depends on the size of E as shown in figure 6 and can be found mathematically as

$$\begin{aligned} D_s = D(r,\sigma) &= \int_0^{2\pi}\int_0^{E/2} \frac{D_0}{\sigma\sqrt{2\pi}} \exp\left(-\frac{r^2}{2\sigma^2}\right) r \, dr \, d\theta \\ &= (I_p t_d/e)\left(1 - \exp\left(-\frac{E^2}{8\sigma^2}\right)\right). \end{aligned} \tag{6}$$

Since E is a variable and increases with the dwell time (t_d), as shown in figure 6, the function of E can be represented very well by $E(t_d - t_0) = C_1(t_d - t_0) + C_2(t_d - t_0)^2$, where t_0 is the dwell time when E is zero, and C_1 and C_2 are the correlation constants. If the mean value of E^2 for the dwell time from 0 to t_d can be defined as

$$E^2_{mean} = \frac{\int_{t_0}^{t_d} [C_1(t_d - t_0) + C_2(t_d - t_0)^2]^2 \, dt_d}{(t_d - t_0)} \tag{7}$$

equation (6) can be rearranged as

$$D_s(t_d) = (I_p t_d/e)\left(1 - \exp\left(\frac{-E^2_{mean}}{8\sigma^2}\right)\right) \qquad \text{for} \quad t_d > t_0 \tag{8}$$

where

$$E^2_{mean} = \tfrac{1}{3}C_1^2(t_0 - t_d)^2 + \tfrac{1}{2}C_1C_2(t_d - t_0)^3 + \tfrac{1}{5}C_2^2(t_d - t_0)^4.$$

3.3. Milling yield formulation

In the present FIB milling, if the dwell time is less than t_0, only one layer, the Au layer, is involved and $E = 0$ and thus equation (3*b*) can be reduced to $N_a = 2CBp_s/b_a^3$. Since the total ion impinging on the target during the whole dwell time (t_d) equals ($I_p t_d/e$), the corresponding milling yield (m_a) to the Au layer can be found as

$$\begin{aligned} m_a &= N_a/(I_p t_d/e) = \left[2CBp_s/b_a^3\right]/(I_p t_d/e) \\ &= 2ep_sBC/\left(I_p t_d b_a^3\right) \qquad \text{for} \quad t_d \leqslant t_0. \end{aligned} \tag{9}$$

Here, since the double charged As^{2+} is used, $e = 3.20 \times 10^{-19}$ C. If the dwell time is longer than t_0, the material in the second layer should be included. By substituting the relationship of $E(t_d - t_0) = C_1(t_d - t_0) + C_2(t_d - t_0)^2$ into equation (3), the corresponding milling yield (m_s) to the Si layer can be found as

$$m_s = N_s/D_s = 4Cp_s[C_1(t_d - t_0) + C_2(t_d - t_0)^2]^2/\left(D_s B b_s^3\right) \quad \text{for} \quad t_d > t_0. \tag{10a}$$

Also, the milling yield (m_a) to the Au layer can be obtained as

$$\begin{aligned} m_a = N_a/(I_p t_d/e - D_s) = 2Cp_s\{B^2 - [C_1(t_d - t_0) \\ + C_2(t_d - t_0)^2]^2\}/\left[(I_p t_d/e - D_s)Bb_a^3\right] \end{aligned} \qquad \text{for} \quad t_d > t_0 \tag{10b}$$

where the numerical value of D_s can be obtained from equation (8).

3.4. Results and discussion

The lattice parameters for Au (b_a) and Si (b_s) can be found in most handbooks and are, respectively, 0.407 86 nm and 0.543 07 nm at the room temperature, reported by Boyer and Gall (1985). It is to be noted that the lattice constants can vary noticeably under different testing temperatures. Using the mathematical correlation of the data shown in figure 6, t_0, C_1 and C_2 can be found as 16.73 ms, 4.8767 nm ms^{-1}, and $-0.053\,83$ nm ms^{-2}, respectively. As shown in figure 6, the correlation between E and the dwell time (t_d) indeed can be represented by a quadratic polynomial. The corresponding correlation coefficient (R) is higher than 0.999, which means the correlation is almost perfectly quadratic. The coefficient R is used to gauge the accuracy of correlation and always lies between -1 and $+1$. A value of zero occurs when the two variables are totally independent of each other, while it reaches 1 when the two variables correlate perfectly, i.e., no deviation from the quadratic curve. In fact, if the real measurement data instead of the quadratic curve are used in the milling yield calculation, the differences in the results are less than 1% and will not be able to be distinguished when the results are plotted as those shown in figure 8.

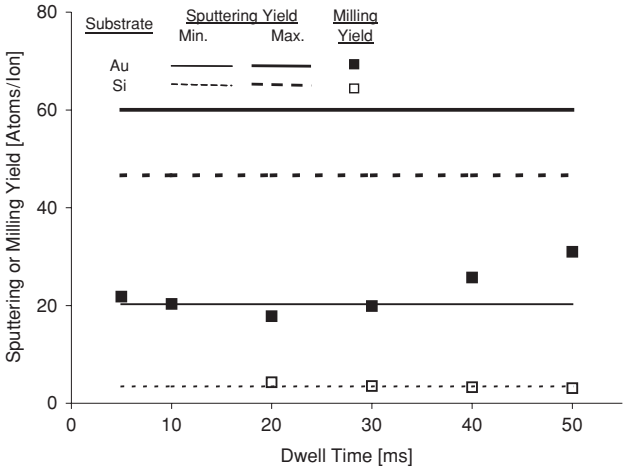

Figure 8. Milling yield estimations compared with sputtering yields at normal incidence and peak.

Based on equations (9) and (10), the correlation values of t_0, C_1 and C_2, and the data of B and C shown in figure 6, the milling yields for both Au and Si can be calculated and their results are plotted against the dwell time in figure 8. The predicted sputtering yields at the normal incidence (lower lines) and peak (higher lines) for Au and Si substrates from figure 3 are also depicted in figure 8 for comparison. In fact, the values between the lower and higher lines are the possible sputtering yields that can take place in milling, As shown in figure 8, the estimated milling yield for the Au substrate varies from 17.8 to 31.0 atoms/ion, while the yield for the Si substrate changes from 3.1 to 4.3 atoms/ion.

Figure 8 shows that at the initial milling stage (say, $t_d < 25$ ms), the milling yields for Au slightly decrease with the increase of the dwell time, varying from 8% higher to 8% lower than the sputtering yield at normal incidence. In milling, material removal or milling yields are mainly dictated by both sputtering and redeposition. It seems that, at the initial stage, the tiny initial decrease of the milling yield of Au should be due to the fact that the redeposition increases slightly with the dwell time, which should be caused by the geometry change of the channel profile. At larger dwell times (say, $t_d > 25$ ms), the milling yield grows monotonically with the dwell time, but is still much smaller than the peak sputtering yield of Au. As shown in figure 5, at larger dwell times, the channel walls in the Au region are tilted significantly; as a result, the milling yield increases because the sputtering yield grows with the incident angle (the tilted angle of the wall). In addition, the sputtered Au from the non-central region can redeposit onto the ridge area much easier than that of the sputtered Si onto the ridges. Consequently, the amount of redeposition to the Au region decreases as the dwell time increases and the decrease of redepositon leads to the increase of milling yield.

As shown in figure 8, in milling of Si, the milling yields also decrease slightly with the increase of the dwell time and reach a steady value at the end of the milling (close to the normal-incidence sputtering yield). The reason for the decrease of the Si milling yield may be just the opposite of the reason for the increase of the milling yield of Au. The decrease of the Si milling yield is caused by the fact that the sputtered Si from the center area should be more difficult than the sputtered Au to be redeposited onto the ridge region; as a result, the amount of redeposition to the central Si region increases with the dwell time. The increase of redepositon leads to the decrease of the milling yield of Si and is more than enough to counterbalance the increase of the sputtering yield due to tilting the channel angle. This eventually leads to the milling yield of Si reaching a stable value which is close to the normal-incidence sputtering yield. It is noted that at the initial stage of milling, it is a single-substrate milling and no Si is involved.

The present finding of the milling yield in the beginning milling state being close to the sputtering yield at normal incidence is consistent with that recently reported by Lugstein *et al* (2003) and Tseng *et al* (2004). In a single scan of channel milling, Lugstein *et al* (2003) used a 50 keV Ga FIB on a single-layer Si substrate and found that the milling yield is almost constant and equal to approximately 2.5 atoms/ion for the milling depth from 100 nm to 700 nm. It can be found from figure 3 that the sputtering yield at normal incidence predicted by TRIM is 3.25 which is close to 2.5 atoms/ion obtained by Lugstein *et al* (2003). Similarly, Tseng *et al* (2004) found that the yield estimation for milling a gold substrate using a 90 keV As^{2+} FIB is roughly equal to the normal sputtering yield of TRIM's prediction and independent of the dwell time. On the other hand, at longer dwell times (i.e., $t_d < 30$ ms) in the present study, the estimated milling yield for the top layer is larger than the normal sputtering yield predicted by TRIM and the magnitude increases with the dwell time, while the milling yield for the bottom layer is still approximately equal to the predicted normal sputtering yield as shown in figure 8. This two-layer effect is more complicated than those observed in single-layer milling.

4. Concluding remarks

FIB milling on a two-layer substrate has been successfully performed. The procedure for preparation of the two-layer substrate is first presented. The guideline for providing uniform input of ion intensity to mill a uniform channel with respect to the milling direction is then discussed. Following the guideline, submicron channels are milled at various dwell times. The cross-sectional profiles are measured by atomic force microscopy and used to characterize the milling operation. A simple formula is developed for the estimation of the milling yield using the AFM measurement data. The reliability of the estimated milling yields is verified by comparing the estimations with the numerically predicted sputtering yield as well as other published results based on single-layer milling.

It has been observed that the channel is milled deeper as the dwell time is increased and the rate of increase of the channel depth is gradually reduced with increasing dwell time. However, the reduction in the rate of increase of the channel depth does not imply that the milling yield is also reduced. Based on the profile measurements, the gradual reduction in the rate of increase of the milling depth is mainly due to the fact that the sputtering yield of the bottom layer, Si, is much smaller than that of the top layer, Au. The impact from the bottom layer becomes more influential for longer dwell times since the

channel is milled deeper into the second layer. Consequently, the rate of increase of the milling depth is reduced as the channel is milled deeper into the Si layer.

The present study indicates that, in the initial milling stage, the milling yields of both layers are close to their respective sputtering yields at normal incidence. This finding is consistent with the observation recently reported based on single-layer milling. The present study also finds that at larger dwell times when the milling gets deeper into the bottom layer, the effects of the two layers become prominent and are not observed when milling a single-layer substrate. At larger dwell times, the milling yield of the top layer grows monotonically with the dwell time due to the increase of the inclination of the associated channel walls and the decrease of redeposition, but it is still much smaller than the peak sputtering yield of the top layer. The present results also suggest that the impact of the redeposition effect increases with the dwell time. It creates a situation that the milling yield of the top layer can increase while the milling yield of the bottom layer can decrease. This leads to the fact that the milling yield of the bottom layer, even at larger dwell times, is close to its normal-incidence sputtering yield.

Similar to the earlier findings based on single-layer milling, the present study has also revealed that FIB milling is an effective process to fabricate V-shaped submicron-scale channels. The study specifically indicates that a range of channel profiles can be obtained by controlling the amount of dose or the dwell time. For example, the width of the channel mouth can be one order of magnitude larger than the beam diameter with a long dwell time. Because of this controllability, in addition to making channel structures, the FIB milling should have great potential for fabricating other types of micron or submicron structures.

Finally, it is understood that the development of the FIB milling technique relies on both theoretical and experimental investigations. In the present study, a simple analytical model is developed to predict the milling yield based on the measured milling profiles. It is more desirable that a numerical model can predict the milling yield as well as the milling profiles. To enhance the modeling capability and reliability, recent modeling efforts, such as those by Nassar *et al* (1998), Boxleitner and Hobler (2001) and Tseng *et al* (2003), along this direction should be encouraged.

Acknowledgments

The authors gratefully acknowledge the support of this study by the US National Science Foundation under grant nos DMI-0002466 and CMS-0115828. Special thanks are given to Professor Zaichun Feng of University of Missouri–Columbia for his encouragement and for providing useful help for this study. The help from David P Pivin, Bharath Leeladharan, Chen-Chuan Fan and Martin Mitan of Arizona State University in conducting this research is specifically acknowledged.

References

Biersack J P and Haggmark L G 1980 A Monte Carlo computer program for the transport of energetic ions in amorphous targets *Nucl. Instrum. Methods* B **174** 257–69

Boxleitner W and Hobler G 2001 FIBSIM-dynamic Monte Carlo simulation of compositional and topography changes caused by focused ion beam milling *Nucl. Instrum. Methods* B **180** 125–9

Boyer H E and Gall T L (ed) 1985 *Metals Handbook* (Metal Park, OH: American Society for Metals)

Budraa N, Jackson H W, Barmatz M, Pike W T and Mai J D 1999 Low pressure and low temperature hermetic wafer bonding using microwave heating *Proc. 12th Ann. IEEE Int. MEMS'99 Conf.* pp 490–2 (also in http://www.fusion.org.uk/stg/bonding2.htm)

Chyr I, Lee B, Chao L C and Steckl A J 1999 Damage generation and removal in the Ga^+ focused ion beam micromachining of GaN for photonic applications *J. Vac. Sci. Technol.* B **17** 3063–7

Creager S E, Hockett L A and Rowe G K 1992 Consequences of microscopic surface roughness for molecular self-assembly *Langmuir* **8** 854–61

Dauksher W J, Resnick D J, Johnson W A and Yanof A W 1994 New operating regime for electroplating the gold absorber on x-ray masks *Microelectron. Eng.* **23** 235–8

Dragoi V, Lindner P, Farrens S and Schaefer C 2003 Bonding 300 mm SOI substrates *Eur. Semicond.* **25** 31–5

Frey L, Lehrer C and Ryssel H 2003 Nanoscale effects in focused ion beam processing *Appl. Phys.* A **76** 1017–23

Fu Y, Bryan N K A, San O A and Hong L B 2000 Data format transferring for FIB microfabrication *Int. J. Adv. Manuf. Technol.* **16** 600–2

Ghandhi S K 1994 *VLSI Fabrication Principles: Silicon and Gallium Arsenide* 2nd edn (New York: Wiley)

Golan Y, Margulis L and Rubinstein I 1992 Vacuum-deposited gold-films: 1. Factors affecting the film morphology *Surf. Sci.* **264** 312–26

Hammiche A, Webb R P and Wilson I H 1994 A scanning-tunneling-microscopy study of thin gold-films evaporated on silicon *Vacuum* **45** 569–73

Hopkins L C, Griffith J E, Harriott L R and Vasile M J 1995 Polycrystalline tungsten and iridium probe tip preparation with a Ga^+ focused ion beam *J. Vac. Sci. Technol.* B **13** 335–7

Hsu T R and Clatterbaugh J 2004 Joining and bonding technologies *MEMS Packaging* ed T R Hsu (London: INSPEC, Institute of Electrical Engineers) pp 23–59

Huang J, Dahlgren D A and Hemminger J C 1994 Photopatterning of self-assembled alkanethiolate monolayers on gold. A simple monolayer photoresist utilizing aqueous chemistry *Langmuir* **10** 626–8

Iida A, Kizaki Y, Fukuda Y and Mori M 1997 Development of repairable Au–Al solid phase diffusion flip-chip bonding *IEEE Trans. Compon. Packag. Manuf. Technol.* C **20** 343–9

Levlin M, Laakso A, Niemi H E-M and Hautojärvi P 1997 Evaporation of gold thin films on mica: effect of evaporation parameters *Appl. Surf. Sci.* **115** 31–8

Li H W, Kang D J, Blamire M G and Huck W T S 2003 Focused ion beam fabrication of silicon print masters *Nanotechnology* **14** 220–3

Lugstein A, Basnar B, Smoliner J and Bertagnolli E 2003 FIB processing of silicon in the nanoscale regime *Appl. Phys.* A **76** 545–8

Madou M J 2002 *Fundamentals of Microfabrication: The Science of Miniaturization* 2nd edn (Boca Raton, FL: CRC Press)

Nassar R, Vasile M and Zhang W 1998 Mathematical modeling of focused ion beam microfabrication *J. Vac. Sci. Technol.* B **16** 109–15

Picard Y N, Adams D P, Vasile M J and Ritchey M B 2003 Focused ion beam-shaped microtools for ultra-precision machining of cylindrical components *Precis. Eng.* **27** 59–69

Reyntjens S and Puers R 2001 A review of focused ion beam applications in microsystem technology *J. Micromech. Microeng.* **11** 287–300

Santamore D, Edinger K, Orloff J and Melngailis J 1997 Focused ion beam sputter yield change as a function of scan speed *J. Vac. Sci. Technol.* B **15** 2346–9

Semaltianos N G and Wilson E G 2000 Investigation of the surface morphology of thermally evaporated thin gold films on mica, glass, silicon and calcium fluoride substrates by scanning tunneling microscopy *Thin Solid Films* **366** 111–6

Stanishevsky A 1999 Focused ion beam patterning of diamondlike carbon films *Diam. Relat. Mater.* **8** 1246–50

Takano J-I, Doyama M and Kogure Y 1997 Simulation of surface diffusion using embedded atom potentials in FCC metals *Structure and Evolution of Surfaces, MRS Symp. Proc.* vol 440 *(Materials Research Society)* pp 115–20

Tseng A A 2004 Recent developments in micromilling using focused ion beam technology *J. Micromech. Microeng.* **14** R15–34

Tseng A A, Insua I A, Park J S, Li B and Vakanas G P 2004 Milling of submicron channels on gold layer using double charged arsenic ion beam *J. Vac. Sci. Technol.* B **22** 82–9

Tseng A A, Leeladharan B, Li B, Insua I A and Chen C D 2003 Fabrication and modeling of microchannel milling using focused ion beam *Int. J. Nanosci.* **2** 375–9

Tseng A A, Tang W C, Lee Y-C and Allen J 2000 NSF 2000 workshop on manufacturing of micro-electro-mechanical systems *J. Mater. Process. Manuf. Sci.* **8** 292–306

Vasile M J, Niu Z, Nassar R, Zhang W and Liu S 1997 Focused ion-beam milling: depth control for three-dimensional microfabrication *J. Vac. Sci. Technol.* B **15** 2350–4

Ward J W 1985 A Monte Carlo calculation of the virtual source size for a liquid metal ion source *J. Vac. Sci. Technol.* B **3** 207–13

Weisstein E W 1999 *Math World* (Boca Raton, FL: CRC Press) (in http://mathworld.wolfram.com/GaussianFunction.html)

Whitesides G M and Love J C 2001 The art of building small *Sci. Am.* **285** 39–47